Novel quantum well, quantum dot, and superlattice heterostructure based infrared detectors

David Z.-Y. Ting[*a], Sumith V. Bandara[1a], Cory J. Hill[a], Sarath D. Gunapala[a], Yia-Chung Chang[2b], H. C. Liu[c], C. Y. Song[c], Alexander Soibel[a], Jason Mumolo[a], Jean Nguyen[a], John K. Liu[a], Sam A. Keo[a], Sir B. Rafol[d], and E. R. Blazejewski[a]

[a]Jet Propulsion Laboratory, California Institute of Technology,
4800 Oak Grove Drive, Pasadena, CA USA 91109-8099
[b]Department of Physics, University of Illinois at Urbana-Champaign,
1110 West Green St., Urbana, IL USA 61801-3080
[c]Institute for Microstructural Sciences, National Research Council of Canada,
1200 Montreal Road, Ottawa, Ontario K1A 0R6
[d] Infravision Systems, Altadena, CA 91001 USA

ABSTRACT

We report work on several quantum structure based infrared detectors. We describe the concept and experimental progress of the quantum well intra-subband photodetector (QWISP), which is closely related to the quantum-well infrared photodetector (QWIP), but uses the dopant-assisted intra-subband absorption mechanism in quantum wells for normal-incidence far infrared/terahertz radiation detection. We describe the concept of the submonolayer quantum dot infrared photodetector (SML QDIP), and report experimental device results on long-wavelength infrared detection, and imaging results from a mega-pixel focal plane arrays, which produced clear infrared images up to 80K. We discuss how superlattice heterostructures, particularly those using unipolar barriers, can offer significant performance advantages over homojunction superlattices in infrared detection. We also summary recent device results on a superlattice heterostructure based barrier infrared detectors (BIRDs).

Keywords: infrared, photodetector, terahertz, quantum well, intra-subband, quantum dot, QWIP, superlattice

1. INTRODUCTION

Recent advances in quantum structure infrared photodetector (QSIP) technologies, including those based on quantum wells, dots, superlattices, and novel heterostructures, have led to the realization of QSIP-based high-performance infrared detectors and large-format focal plane arrays. In this paper, we describe our research progress in three types of QSIPs: (1) the quantum well intra-subband photodetector (QWISP) for far infrared/terahertz radiation detection, (2) the submonolayer quantum dot infrared photodetector (SML QDIP), and (3) superlattice heterostructure based barrier infrared detectors (BIRDs).

* David.Z.Ting@jpl.nasa.gov; Ph: +1.818.354.1549; FAX: +1.818.393.4663
[1] Present address: Night Vision & Electronic Sensors Directorate, Ft Belvoir, VA 22060 USA
[2] Present address: Research Center for Applied Sciences, Academia Sinica, Taipei 11529 Taiwan

Infrared Technology and Applications XXXV, edited by Bjørn F. Andresen, Gabor F. Fulop, Paul R. Norton
Proc. of SPIE Vol. 7298, 729805 · © 2009 SPIE · CCC code: 0277-786X/09/$18 · doi: 10.1117/12.818879

2. QUANTUM WELL INTRA-SUBBAND INFRARED PHOTODETECTOR (QWISP)

There has been considerable interest in far infrared (FIR) and terahertz (THz) sources and detectors in recent years. FIR/THz radiation detection has already been demonstrated in compact semiconductor heterostructure devices such as the quantum cascade detector (QCD) [1], the heterojunction interfacial workfunction internal photoemission (HEIWIP) detector [2, 3], and the quantum well infrared photodetector (QWIP) [4, 5]. Recently, we proposed an alternative device concept called the Quantum Well Intra-Subband Photodetector (QWISP), and studied the effectiveness of QWISP theoretically by comparing it with the far-IR/THz quantum-well infrared photodetector (QWIP) [6, 7, 8]. As illustrated in Fig. 1 (a) and (b), compared to the long-wave infrared (LWIR) QWIP, the FIR/THz QWIP has a wider quantum well for the small inter-subband transition energy, and a lower barrier to keep the upper state in resonance with the top of the barrier in accordance with the bound-to-quasibound (B-QB) QWIP design rule [9]. Because the ground-state energy is very close to the top of the barrier, to limit dark current, FIR/THz QWIPs require low doping, which leads to low quantum efficiency [10]. The QWISP addresses this problem by using the intra-subband absorption mechanism instead. A study of discrete dopant effects in LWIR QWIP showed that dopant impurity scattering could induce large normal-incidence FIR absorption [11]. However, this effect cannot be exploited in LWIR QWIPs because the electrons photoexcited via intra-subband transitions do not have sufficient energy to escape from the well to contribute to photocurrent. The QWISP, illustrated in Fig. 1(c), can be viewed as a modified LWIR QWIP where the barrier has been lowered to allow the electrons photoexcited by FIR/THz radiation through intra-subband absorption to escape into the continuum and carry current. The QWISP utilizes the dopant-assisted intrasubband absorption mechanism in quantum wells for normal-incidence FIR/THz radiation detection. Like the QWIP, the QWISP is a compact device which could be implemented in GaAs technology. It does not require barriers with very low aluminum content, and is compatible with focal-plane array technology. QWISP's strong normal incidence absorption characteristics eliminate the need for

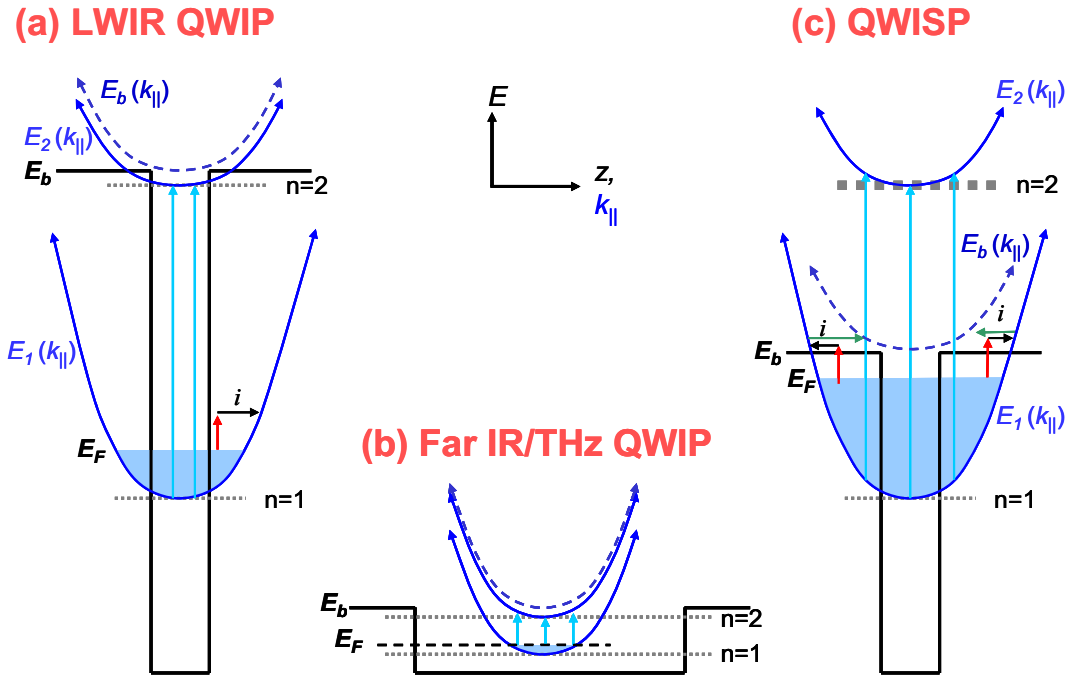

Fig. 1 Schematic illustrations of the energy band diagrams [band edge energy E vs. position z along the growth direction] and the energy dispersions plots [parabolic curves showing quantized state energy levels vs. wave vector $k_{||}$ along an in-plane (x- or y-) direction] for (a) an LWIR QWIP, (b) a far IR/THz QWIP, and (c) a QWISP. Note that the band diagrams and the dispersion plots share the same vertical axis (energy) but different horizontal axes. Inter-subband and intra-subband transitions are indicated by light-blue and red arrows, respectively. The 2D Fermi sea is indicated by the light-blue shaded region.

the optical gratings, thus greatly simplifying the focal plane array fabrication process. For the QWIP, the intersubband energy difference decreases as the wavelength becomes longer. Therefore the ground state doping level has to be kept sufficiently low so that the Fermi level cannot overtake the first excited state, and hence the quantum efficiency for far-IR QWIP decreases as the wavelength becomes longer. On the other hand, the QWISP is ineffective at shorter wavelength because the impurity scattering mechanism can only supply a limited amount of momentum change for intra-subband transition. Our theoretical studies showed that while the QWISP's performance improves as we increase the detection wavelength past 60 μm, the QWIP's performance becomes better as we decrease the detection wavelength to below 60 μm. In this sense the QWISP and QWIP are complementary quantum well IR detector technologies covering different regions of the infrared spectrum.

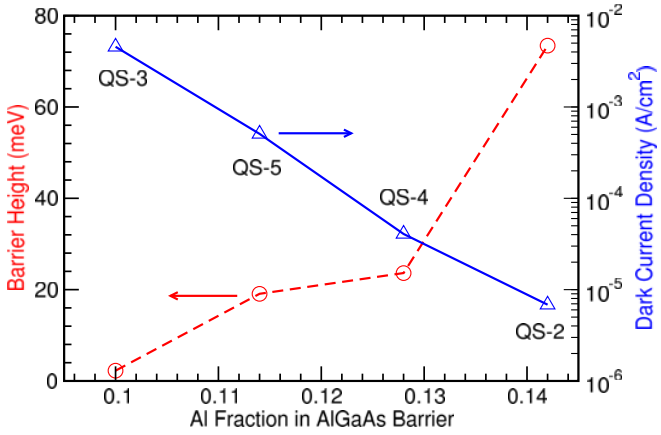

Fig. 2 Low temperature dark current density and activation energy for four GaAs/AlGaAs QWISP devices with different barrier compositions. The devices are mesas with 500 μm on the side. The dark current is measured at ~ 10K.

We performed dark current measurement and activation analysis on four GaAs/AlGaAs QWISP samples, and the results are presented in Fig. 2. All samples use 50 Å quantum wells doped to $5\text{x}10^{18}$ cm^{-3}, n-type. The Al contents in the AlGaAs barriers of the four samples are 0.1, 0.114, 0.128, and 0.142. Our previous theoretical analysis [6], which took into account the effect of discrete dopant potential, showed Fermi level lowering (band gap renormalization) effects under high doping conditions due to the merging of the impurity band and the n=1 subband. However, the measured Fermi level lowering, as deduced from activation energy analysis, is even larger than predicted. We believe this is due to many-body effect induced band gap renormalization [12]. Fig. 3 shows the Fermi level for a QWISP structure calculated using the simple formula

$$E_F = E_1 + \frac{\hbar^2 k_F^{\,2}}{2m^*} = E_1 + \frac{\pi\hbar^2 n_{2D}}{m^*},$$

where E_1 is the quantum well ground state energy and n_{2D} is the 2D doping density in the well. The Fermi levels computed by numerical supercell simulations [6,7,8] using discrete dopants are shown by the asterisk symbols in Fig. 3. Corrections due to exchange interaction (computed using formulation given in References 13 and 14,) and due to band non-parabolicity are also shown.

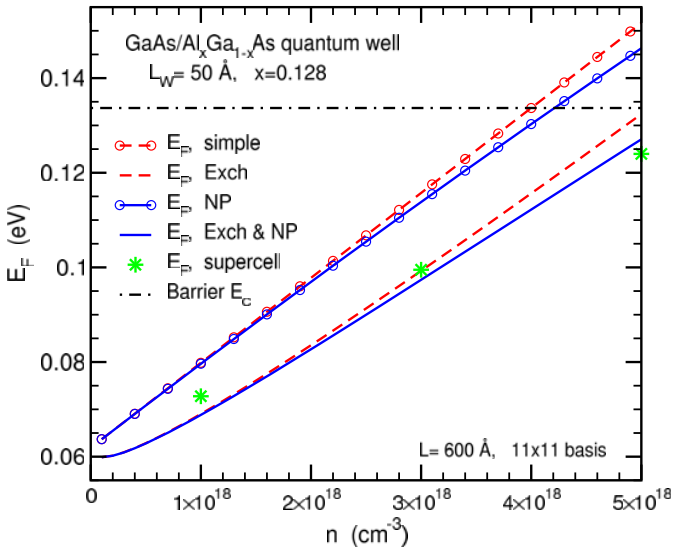

Fig. 3 The Fermi level of a QWISP structure as a function of 3D doping density, calculated with and without exchange interaction and band non-parabolicity effects. Result from numerical supercell simulations that model the effects of band tailing due to discrete dopants (but not many-body effects) are shown by "*" symbols. For reference, the conduction band edge of the AlGaAs barrier is indicated by the dash-dot line.

The importance of these corrections is clearly seen for the case of $n=5\times10^{18}$ cm^{-3}, where the Fermi level without the exchange and non-parabolicity corrections would have been above the AlGaAs barrier. Note that the calculated Fermi level lowering due to exchange interaction and non-parabolicity corrections has approximately the same size as that due

to band tailing as computed by numerical supercell simulations using discrete dopants. Adding the two effects together brings the calculated Fermi level lowering to much better agreement with experimentally measured values.

Room temperature FTIR measurements on QWISP samples showed broad absorption peak centered at ~ 11 μm, corresponding to (n=1 to n=2) intersubband absorption of side-incidence light, as depicted in Fig. 1(c). In addition, we also find response at much longer wavelengths, which we tentatively attribute to intra-subband absorption. Fig. 4 shows preliminary data on far infrared response from the QWISP sample with an $Al_{0.128}Ga_{0.872}As$ barrier. The photo-response peak found at ~ 45 μm corresponds approximately with the activation energy, although we caution that the actual peak position may be different, as the measurement is performed on a backside illuminated sample, where the effect of phonon absorption in the GaAs substrate is substantial. Work in progress on front-side illuminated samples should provide clarification.

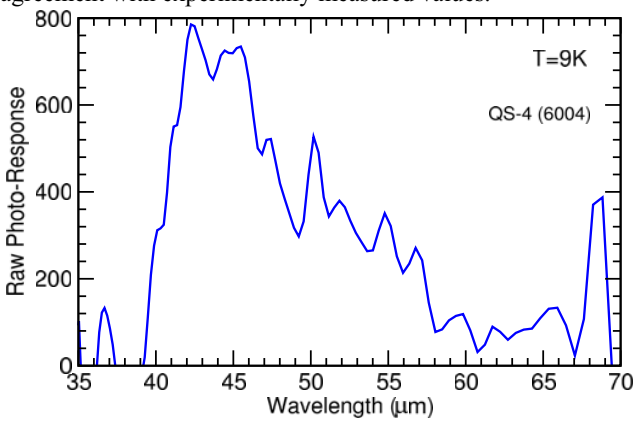

Fig. 4 Raw photo-response as a function of wavelength for a GaAs/AlGaAs QWISP device. The Al content in the barrier is x=0.128. The doping level in the 50 Å well is 5×10^{18} cm^{-3}.

3. SUBMONOLAYER QUANTUM DOT INFRARED PHOTODETECTOR (SML-QDIP)

It has been predicted that quantum dot infrared photodetectors (QDIPs) with small dot size, high dot density and uniformity could outperform quantum well infrared photodetectors (QWIPs) [15,16], due to their normal incidence absorption properties and reduced intersubband scattering. QDIPs studied to date are generally based on quantum dots formed via the Stranski-Krastanow (S-K) growth mode [17]. Fig. 5 illustrates an InAs/GaAs QDIP structure with S-K QDs, typically formed by depositing 2 to 3 monolayers of InAs on lattice mismatched GaAs substrates. The first monolayer or so of the InAs deposited forms a 2D wetting layer, which makes up a significant fraction of the InAs deposited for dot formation, but does not contribute to normal incidence absorption. The dimension of the quantum dot that is the most relevant to normal-incidence absorption is the lateral quantization dimension: specifically, the base width of the quantum dot. We suggest that monolayer-thick, isolated InAs islands embedded in GaAs could still retain the key properties of normal-incidence absorption and reduced LO phonon scattering for 3D confined structures. Such structures are in fact routinely made by depositing fractional (typically 1/2 or 1/3) monolayers of a semiconductor on top of a lattice mismatched substrate [18]. In particular, the InAs/GaAs submonolayer (SML) QD system is well-characterized [19], and is used in vertical cavity surface-emitting lasers (VCSELs) [20] and disk lasers [21]. The use of SML QDs instead of S-K QDs has the advantage that, whereas typically 2-3 monolayers of InAs is needed for a single layer of S-K QD formation, only 1/3 to 1/2 monolayer is needed for SML QD. The reduction in the amount of lattice mismatched material (InAs) used per layer of QD formation means that the material is less strained, and therefore more

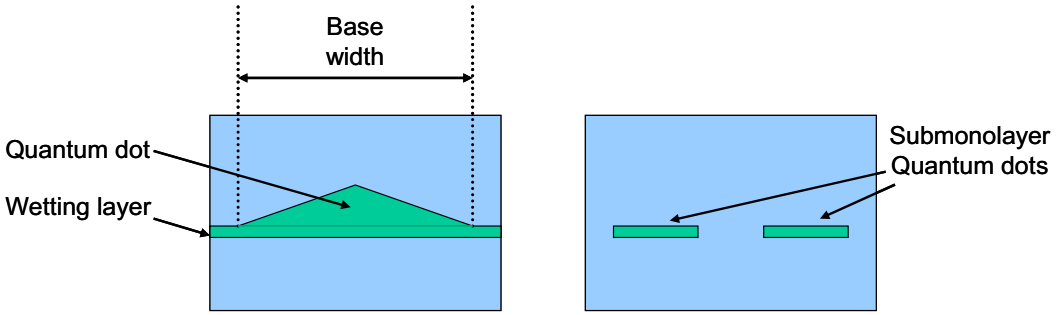

Fig. 5 The left panel illustrates a Stranski-Krastanow quantum dot, consisting of pyramid-shaped quantum dot resting on a wetting layer. The right panel shows submonolayer (SML) quantum dots.

stacks of QD layers can be formed. In contrast to the S-K QD, where typically only ~60% of the strained material deposited is used for building 3D structures, in the SML QD, all of the strained material deposited is used in building 3D structures. SML QDs can be realized in a variety of insert/host matrix semiconductors [22,23]. The lateral dimensions of SML QDs can be quite small (5 – 10 nm), and the dot areal density can be quite high [19, 22]. By controlling the inter-layer spacer thickness, multiple SML-QD layers can be stacked with vertical alignment [24], yielding device design flexibility. These considerations led us to the concept of the SML-QDIP as an alternative to S-K QD based QDIPs.

We fabricated SML QDIP test devices from two different samples. The structures consist of InAs SML QD layers embedded in GaAs quantum wells (QWs) surrounded by AlGaAs barriers. This is rather similar to the DWELL structures we reported previously [25], with the main difference being that the S-K QDs are replaced by SML QDs. For the SML QD, the vertical dimension is only a single monolayer thick, and therefore the quantization energy associated with the vertical direction is high. For a simple QDIP structure with InAs SML QD embedded in GaAs, the ground state would be too close to the GaAs barrier conduction band edge, leading to high levels of dark current. Therefore the DWELL structure is chosen because it provides a taller (AlGaAs) barrier. The width of the GaAs quantum well is 51 Å. Each quantum well contains two symmetrically placed SML QD layers, formed by depositing ½ monolayer of InAs on GaAs. The SML QD layers are located at approximately 14 Å from the center of the quantum well. The quantum well are doped to 5×10^{17} cm^{-3}, n-type. Each sample contains 30 quantum wells, therefore there are 60 SML QD layers per sample. The width of the AlGaAs inter-well transit region is approximately 500 Å. The Al fraction of the AlGaAs barriers in samples SMD 1-1 and SMD 1-2 are 0.20 and 0.16, respectively.

We fabricated 200 μm × 200 μm devices for dark current and responsivity measurements. Fig. 6 shows the measured dark current densities as functions of detector temperature for SMD 1-1 and SMD 1-2 under various operating biasing conditions. Separate 8-pass polished waveguide structures were fabricated for absorption measurement using unpolarized light [26]. Fig. 7 shows the measured room temperature absorption (internal) quantum efficiency (Q.E.) from the two SML QDIP samples. For SMD 1-1 and 1-2, respectively, the room temperature absorption Q.E. peaks occur at 8.9 μm and 10.9 μm, with peak values of 6.8% and 7.5% (without correction for transmission

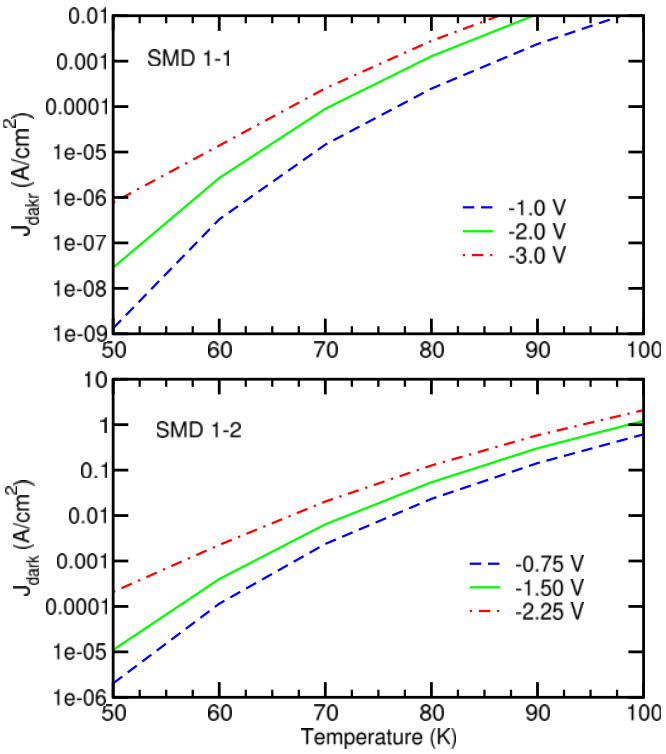

Fig. 6 Dark current density as functions of temperature under various biasing conditions for two SML QDIP samples, SMD 1-1 and SMD 1-2, described in the text.

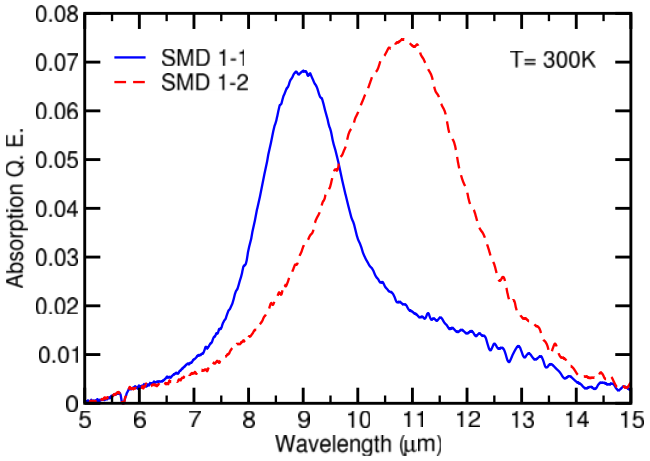

Fig. 7 Measured room temperature internal absorption quantum efficiency for two SML QDIP samples, SMD 1-1 and SMD 1-2.

losses). This compares quite favorably with our previously reported DWELL structure (consisting of 30 stacks of InAs S-K QD embedded in InGaAs QW, also doped to 5×10^{17} cm^{-3}, surrounded by GaAs barriers), for which the absorption Q.E. peaked at 8.0 μm, with a peak value of 2.7% [25].

Fig. 8 shows the normal incidence and 45° incidence responsivity measured for SMD 1-2. (Responsivity results for SMD 1-1 can be found in Reference 28.) The responsivity peak occurs at ~10 μm, with peak values of 178 mA/W and 543 mA/W at -2.25 V for the normal- and 45°-incidence configurations, respectively. The ratios of the normal incidence to 45° incidence response under -0.75V and -2.25V applied bias are 43% and 33% respectively. These values are considerably higher than that found for the typical GaAs/AlGaAs QWIP (~10%), and may be attributed to the 3D nature of the wave function induced by the presence of the InAs SML QDs. We note, however, that other explanations, such as finite cavity edge effects [27], could also be responsible for the relatively large ratio observed here. SMD 1-1, with peak detection wavelength of 8.5 μm, reached background-limited (300K, f/2 optics) infrared photodetection (BLIP) at T ~ 60K under -1V bias, with a black-body D^* value of 6.7×10^{10} Jones. This compares quite favorably with our previously published DWELL detector, which reached BLIP at T ~50K under -1V bias, with a shorter peak detection wavelength of 8.1 μm [25].

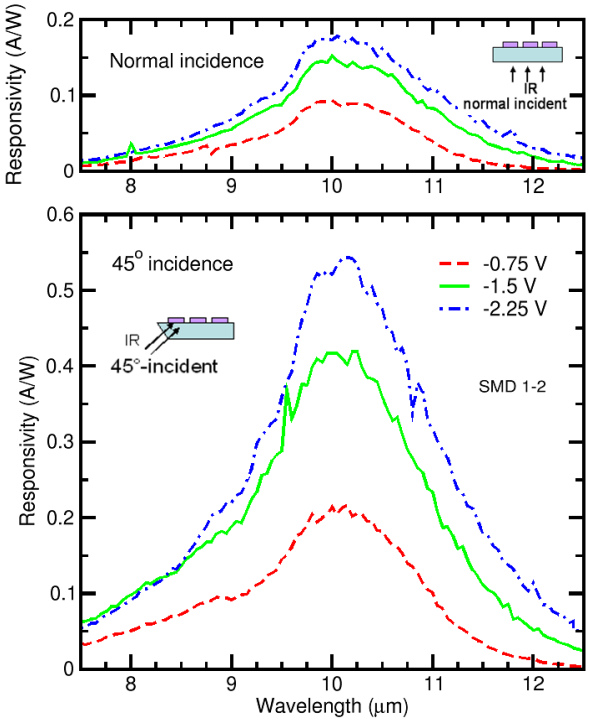

Fig. 8 Normal incident (top panel) and 45-degree incidence (bottom panel) responsivity of an SML-QDIP, Sample SMD 1-2, measured under several applied biases.

Several megapixel (1024×1024) focal plane arrays (FPAs) were made from another SML QDIP sample (SMD 2-1), which is similar to SMD 1-2, except it contains 40 quantum wells, and uses (taller) $Al_{0.2}Ga_{0.8}As$ barriers. The peaks response for SMD 2-1 is found at 7.8 μm. Figure 3 shows two sample images taken through f/2 optics using two

Fig. 9 Images taken with two SML QDIP FPA using f/2 optics. The left panel shows an 800×800 image cropped from a megapixel image taken with FPA Q-1017 at 45K. The right panel shows a 1024×1024 image taken with FPA Q-1018 taken at 80K.

different FPAs. The image on the left is taken at 45K, and shows very good dynamic contrast. The image on the left is taken at 80K, and is still quite clear. The FPAs showed good uniformity and operability, with estimated noise equivalent temperature difference (NETD) of 22mK, 28mK, and 33 mK, respectively, at 50K, 60K, and 70K. Details of the SML QDIP have been reported elsewhere [28].

4. SUPERLATTICE HETEROSTRUCTURE BARRIER INFRARED DETECTORS

In this section, we present a brief history of the antimonide superlattices, examine how band structure influences device properties, discuss the use of unipolar barrier, and present some recent results from the Jet Propulsion Laboratory.

4.1 A brief history of the antimonide superlattice

In 1977, Sai-Halasz, Tsu, and Esaki [29] proposed a new type of bilayer semiconductor superlattice in which the lower conduction band (CB) edge is located in one host material, while the higher valence band (VB) edge is in the other. In this kind of superlattice, the wave functions of the lowest conduction subband and the highest valence subband are localized in the two different host semiconductors (spatially delocalized), and therefore the positions of the CB edge and the VB edge can be tuned independently. It was suggested that this type of superlattice could be realized using InGaAs/GaSbAs. It was also pointed out in particular that the CB edge of InAs was expected to be lower than the VB edge of GaSb (in what is now called the broken-gap band alignment), and this would lead to interesting behavior since the superlattice CB and VB states are close in energy and could therefore interact. This new type of superlattice, in which the band gaps of the two host semiconductor are either in a staggered or in a broken-gap alignment, was called "type II", to distinguish it from the "type I" superlattice original proposed by Esaki and Tsu [30], in which the band gaps are in a nested alignment. In the literature, "type-II broken-gap" is sometimes referred to as "type-III", to distinguish it from "type-II staggered" [31, 32]. H. Kroemer advocates using only the descriptive names of nested (or straddling), staggered, and broken-gap (or misaligned), and doing away with numerical designation of type I, II, and III altogether. In 1978, Sai-Halasz and co-workers demonstrated infrared absorption in an InAs/GaSb superlattice with a ~0.35 eV band gap [33].

The development of the antimonide superlattice as an infrared detector material was influenced by HgCdTe (MCT) in an interesting way. In 1979, Schulman and McGill proposed the use of the CdTe/HgTe superlattice as an infrared material, with possible uniformity advantages over the MCT alloy [34]. Their paper mentioned the use of the InAs/GaSb superlattice as an alternative infrared material, but expressed concerns for the small optical matrix element due to the fact that electron and hole wave functions of the states involved in the infrared transition are spatially separated in a type-II superlattice. Later, in 1983, Smith, McGill, and Schulman revisited the theory of CdTe/HgTe superlattices, and pointed out some key advantages of superlattices over bulk materials for infrared detection: (1) superlattices have weaker cutoff wavelength dependence on composition than the MCT alloy, and are therefore less susceptible to variations due to composition fluctuation, (2) superlattices have reduced p-side diffusion current due to the larger electron mass, and, (3) superlattice tunneling lengths are shorter than for MCT alloys with the same band gap, and therefore have reduced band-to-band tunneling [35]. These same properties apply to the InAs/GaSb superlattice as well. To address the issue of small oscillator strength in InAs/GaSb superlattices, in 1987 Smith and Mailhiot (former McGill student) proposed the type II InAs/GaInSb strained layer superlattice (SLS) infrared detector [36]. The SLS has larger optical matrix elements than the InAs/GaSb superlattice. Although the optical matrix element of the type-II SLS is still smaller than that in bulk MCT, its absorption coefficient is comparable to that of MCT because of the higher joint density of states. The electron effective mass for a 10 μm cutoff SLS is ~0.04 m_0 (0.0088 m_0 for MCT of comparable cutoff wavelength), which is large enough to reduce band-to-band tunneling, and still small enough to provide good electron mobility. In 1990, Miles, Chow, Schulman (all former McGill students) and McGill experimentally demonstrated LWIR absorption in InAs/GaInSb strained layer superlattices [37].

D. L. Smith also postulated that Auger recombination rates in superlattices should be lower than those in bulk semiconductors due to the splitting of the heavy hole (hh) and light hole (lh) bands, and the larger electron effective mass. Smith communicated the idea to McGill [38], who in turn stimulated H. Ehrenreich's group to perform detailed calculations to put this concept on a firm theoretical basis. In 1992, Grein, Young, and Ehrenreich showed that p-type Auger lifetimes in a 11 μm cutoff InAs/InGaSb SLS at 77K could be 3-5 orders of magnitude longer than those of bulk

MCT with the same gap [39]. Experimental measurements of Auger lifetime enhancement in InAs/GaInSb superlattices were reported in 1994 [40]. As the material quality of antimonide superlattices improves, and defect related dark currents decrease, the long Auger lifetimes could yield real advantages in LWIR antimonide superlattice detectors.

It is clear that one of the key proponents of antimonide superlattice infrared detectors was Tom McGill, who passed away unexpectedly in March 2009. In addition to the work mentioned above, Prof. McGill encouraged his former students and associates to work on fundamental studies that are important for the development of this technology. Some of the work includes the theoretical calculation of InAs/GaSb optical properties using a realistic band structure model [41], the influence of interface types [42], and cross-sectional scanning electron microscopy studies of antimonide superlattices [43,44]. Prof. McGill was a tireless champion of advanced solid-state device physics and applications. In particular, his contributions were crucial to the development of antimonide superlattice infrared detector technology.

The work was carried further by Fuchs and co-workers at Fraunhofer IAF. Their demonstration of high-performance InAs/GaInSb infrared photodiodes in 1997 [45] generated strong interest in the antimonide superlattices. Since then, the area has seen rapid progress, with photodetector and FPA results reported by many groups [46,47,48,49,50,51]. It is interesting to note that while the oscillator strength of the InAs/GaSb superlattice is not as strong as that of the InAs/GaInSb SLS, both types of antimonide superlattices are being actively investigated today. In particular, Prof. Razeghi's group at Northwestern has been reporting results on the InAs/GaSb superlattice since 1998 [52]. While the oscillator strength of the InAs/GaSb superlattice is weaker, in common with the SLS it also has a higher joint density of states than bulk semiconductors, and therefore has an adequately large absorption coefficient. The InAs/GaSb superlattice, which uses unstrained and minimally strained binary semiconductor layers, may also have material quality advantages over the SLS, which uses a strained ternary semiconductor (GaInSb). Most recently, the use of superlattice heterostructures has resulted in very substantial performance gains over homojunction devices. In the future, we expect high performance superlattice detectors to be primarily of heterostructure design.

4.2 Band structure considerations

In constructing superlattice based infrared detector structures, special considerations should be given to the absorber superlattice intrinsic properties, many of which are revealed by band structure. Fig. 10 shows the band structure of a typical LWIR broken-gap superlattice, calculated using an enhanced effective bond orbital model [53]. The main features of the superlattice band structure that distinguishes it from that of the typical bulk semiconductor are that (1) the splitting of the highest heavy hole band (HH1) and the highest light hole band (LH1) at the zone center, and, (2) the HH1 band is nearly dispersionless along the growth direction. While the infrared absorption edge is determined by the gap between the lowest conduction band (CB1) and the HH1 band, the electron effective mass is determined by the CB1-LH1 gap. In unstrained bulk semiconductors, the two gaps are the same. In the superlattice, the larger CB1-LH1 gap leads to a large electron effective mass, which is beneficial for reducing band-to-band tunneling. Both the dispersionless HH1 band structure and the increased electron effective mass contribute to a larger joint density of states (JDOS). This results in a larger absorption coefficient, which, to first order, is directly proportional to the JDOS. This helps to compensate for the small optimal

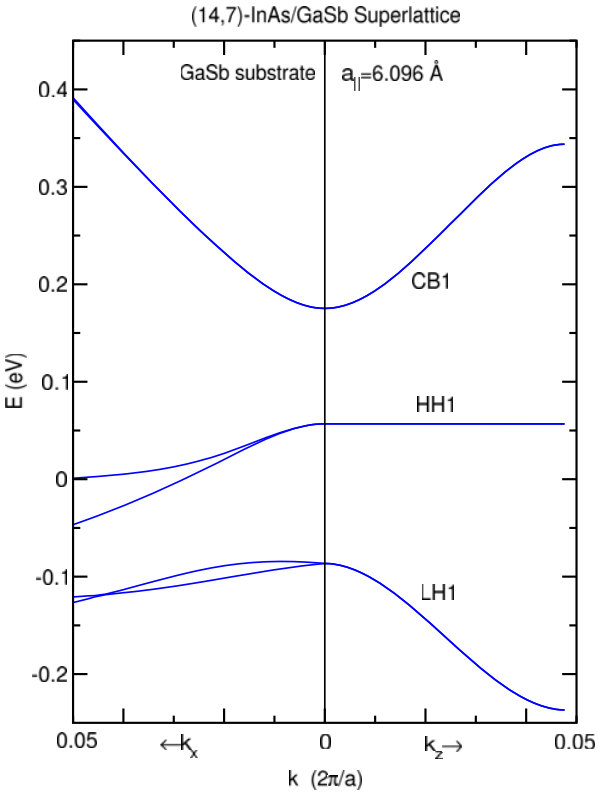

Fig. 10 Conduction and valence band structure emanating from the zone center along an in-plane direction (k_x) and the growth direction (k_z), with k_y = 0, for a long wavelength infrared superlattice. Each superlattice period consists of L_z=21 monolayers (MLs), with 14 MLs of InAs and 7 MLs of GaSb.

matrix element disadvantage inherent in type II superlattices. As mentioned previously, the splitting of the HH1 and LH1 bands can also help in reducing Auger recombination.

The band structure reveals important information about carrier transport properties which can affect detector design. We note that the CB1 band shows strong dispersion along both the growth (z) and an in-plane direction (x), while the HH1 band is highly anisotropic and appears nearly dispersionless along the growth (transport) direction. We expect the electron and hole density of states to be 3D- and 2D-like, respectively. The calculated conduction and valence subband zone center effective masses along the x and z directions are: $m_c^x* = 0.021m_0$ and $m_c^z* = 0.021m_0$, and $m_{hh1}^x* = 0.031m_0$ and $m_{hh1}^z* = 38m_0$. Recalling that carrier group velocity is given by $\mathbf{v} = \nabla_{\mathbf{k}} E(\mathbf{k}) / \hbar$, where $E(\mathbf{k})$ describes the band structure, we would expect very low hole mobility and diffusivity along the growth direction. Therefore, for this LWIR superlattice absorber, detector designs based on hole transport would be rather unfavorable. Moreover, in general low mobility of holes can also slow down the electrons, since excess electrons and holes are coupled through coulomb interaction (ambipolar transport). We should point out that the hole mobility for MWIR superlattices are not nearly as poor. The calculated conduction and valence subband zone center effective masses for the (8,6)-InAs/GaSb MWIR superlattice along the x and z directions are: $m_c^x* = 0.025m_0$ and $m_c^z* = 0.024m_0$, and $m_{hh1}^x* = 0.037m_0$ and $m_{hh1}^z* = 1.85m_0$. Note that the MWIR superlattice HH1 effective mass is ~20 times smaller than for the LWIR superlattice.

Even for the LWIR superlattice, a closer look at the HH1 band structure reveals that the hole velocity may not be as poor as first appeared. The graph on the left side of Fig. 11 shows that in the LWIR superlattice, for $k_y = 0$, the HH1 band

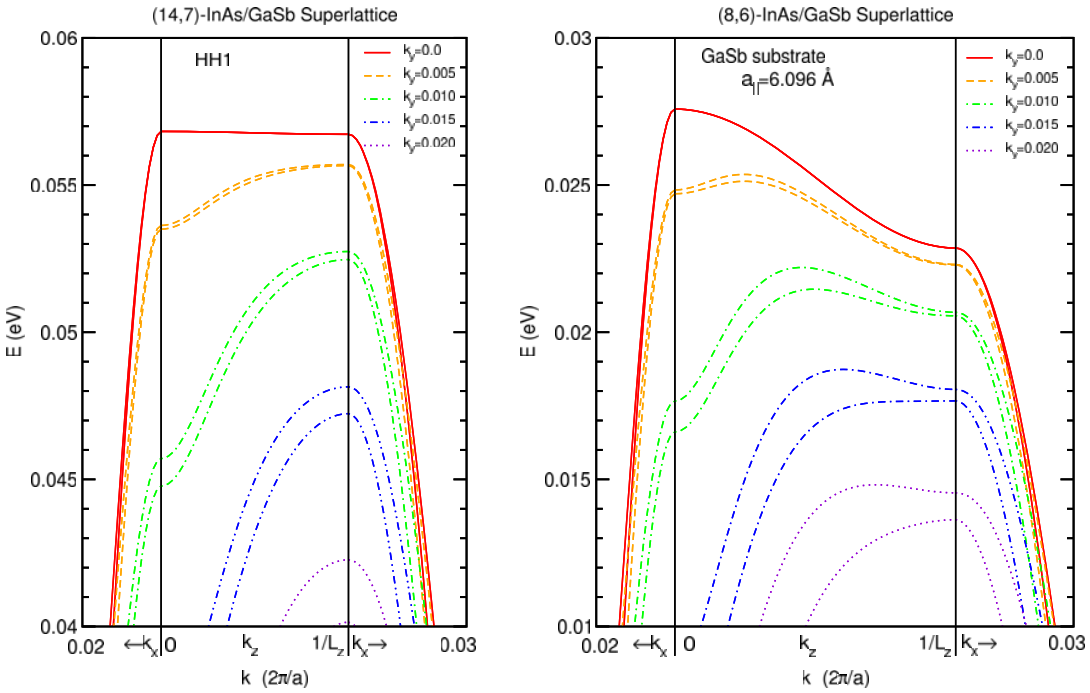

Fig. 11 (14,7)-InAs/GaSb superlattice (left) and (8,6)-InAs/GaSb superlattice (right) HH1 subband band structure. In each graph, the central panel shows band structure along the growth direction (k_z) from the reduce zone center to the zone boundary. The side panels show the continuation of the band structure plotted along the in-plane direction k_x. The HH1 bands for several k_y values are plotted. In each graph, L_z is the number of monolayers in each period of the superlattice (21 and 14, respectively, for the graphs on the left and right side). For reference, the value of $k_B T$ is ~14 meV at T=80K.

has very little dispersion along k_z (the growth direction), with maximum occurring at the center of the reduced Brillouin zone. But as the result of interaction with other subbands, the HH1 band dispersion along the growth direction becomes appreciably larger as the in-plane momentum (k_y) increases; the band maximum along the k_z direction quickly switches from the reduced zone center to the zone boundary. At lower temperatures, we expect holes to occupy the less dispersion portions of the HH1 band, for which the hole density of states is more 2D-like, and hole velocities along the growth direction are low. At higher temperatures, we expect the more dispersive parts of the HH1 to be occupied also. The thermalized holes would occupy the part of the density of states that is more 3D-like, and would attain higher velocities. We note that there is tentative indirect experimental evidence from superlattice infrared detector dark current analysis that the hole density switches from 2D- to 3D-like with increasing temperature, as reported elsewhere [54]. The right side of Fig. 4 shows the corresponding HH1 band structure plot for the (8,6)-InAs/GaSb MWIR superlattice. Note that in this case, the HH1 band shows a reasonable amount of dispersion even at $k_y = 0$, and its hole transport properties should be much better than that of the LWIR superlattice.

4.3 Unipolar Barriers

Unipolar barriers, barriers that can block one carrier type (electron or hole) but allow the un-impeded flow of the other, as illustrated in Fig. 12, can be used to enhance the performance of semiconductor devices. The much celebrated concept of the double-heterostructure (DH) laser, which makes uses a pair of complementary unipolar barriers, was first described in 1963 [55, 56], soon after the birth of the idea of heterostructure devices itself. Unipolar barriers are also used to enhance infrared detector performance. A unipolar barrier can be used to impede the flow of majority carrier dark current in photoconductors [57]. A DH detector design, depicted in Fig. 12, can be used to reduce diffusion dark current emanating from the diffusion wings surrounding the absorber layer [58]. The nBn [59, 60] (see Fig. 12) or XBn [61] detector structure uses a unipolar barrier to suppress dark current associated with Shockley-Read-Hall processes without impeding photocurrent flow, and to suppress surface leakage current [60]. In general, unipolar barriers can be used to implement the barrier infrared detector (BIRD) architecture for increasing the collection efficiency of photo-generated carriers, and reducing dark current generation without impeding photocurrent flow.

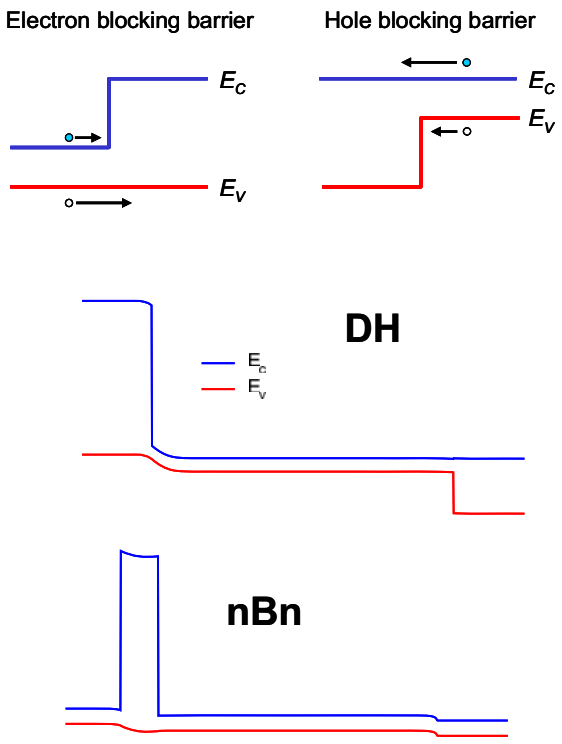

Fig. 12 Schematic illustrations of electron- and hole-blocking unipolar barriers, and two examples of unipolar barrier based device structure: the double-barrier heterostructure (DH), and the nBn structure.

In practice, unipolar barriers are not always readily available for the desired infrared absorber material, as both the absorber and barrier materials require (near) lattice matching to available substrates, and the proper band offsets must exist between the absorber and the barrier. Considerable effort and ingenuity may be required find work-around if an ideal match cannot be found [58]. The nearly lattice-matched InAs, GaSb, AlSb material system, which can be epitaxially grown on GaSb or InAs substrates, is well suited for implementing BIRD structures. With the availability of type-I nested, type-II staggered (straddling), and type-II broken-gap (misaligned, or type III) band offsets between the GaSb/AlSb, InAs/AlSb, and InAs/GaSb material pairs, respectively, there is considerable flexibility in forming a rich variety of alloys and superlattices.

The type-II broken-gap InAs/Ga(In)Sb superlattice can be used as mid- or long-wavelength infrared absorber.

Superlattices or alloys build from the InAs/GaSb/AlSb material system can also be tailor-designed to build matching unipolar barriers. In particular, the ability to tune the positions of the conduction and valence band edges independently in a type II superlattice is especially helpful in the design of unipolar barriers. Examples of the broken-gap superlattice based BIRDs are the superlattice nBn [62], the superlattice DH [63,64], and the graded-gap W-superlattice based DH structure [65].

4.4 Recent JPL Results

Using BIRD designs with unipolar barriers, we have been able to improve the LWIR superlattice detector significantly over superlattice infrared detectors based on homojunction designs. Typically, we are able to reduce the dark current density substantially without cutting back on the photo-response very much. As an example, a ~10 μm cutoff (defined by 50% peak responsivity) large area device (220 μm × 220 μm in size) without anti-reflection coating using unipolar barrier based design exhibits a responsivity of 1.5 A/W and a dark current density of $\sim 1\times10^{-5}$ A/cm^2 at 77K under 0.2 V bias. The device has a zero-bias dynamic resistance-area product of R_0A =14,000 ohm-cm^2 at 77 K, which is the highest value for a 10μm cutoff SL detectors reported to date. However we need to point out that while R_0A is useful for characterizing Johnson noise limited photovoltaic detectors operating near zero bias, it is less relevant for this detector, which operates at a higher bias where shot noise dominates. Here it is more appropriate to examine the dark current density under the operating bias for determining detector noise spectrum. Therefore, we report shot-noise limited black-body D^*, where the noise spectrum is determined by the dark current and the photocurrent integrated over the 8 μm to 10 μm spectral range (the overlap between the atmospheric window and the detector cutoff). We take the background limited infrared photodetection (BLIP) condition to be where the dark current is ¼ of the photocurrent. Under 0.2 V, the detector reaches 300 K BLIP operation at 86 K with a black-body BLIP D^* value of 1.1×10^{11} cm-Hz$^{1/2}$/W for f/2 optics. For 300K background with 2π field of view, the devices shows a BLIP temperature of 101 K with a black-body BLIP D^* value of 2.6×10^{10} cm-Hz$^{1/2}$/W. A full description of the device results will be reported elsewhere [66].

5. SUMMARY

We report work on several quantum structure based infrared detectors. We showed that instead of using intersubband transitions in the quantum well infrared photodetector (QWIP) for LWIR detection, we can exploit the dopant-assisted intrasubband absorption mechanism in quantum well for normal-incidence far infrared/terahertz radiation detection in the quantum well intra-subband photodetector (QWISP). We also showed that apart from the standard Stranski-Krastanow (S-K) quantum dots for infrared detection, the submonolayer quantum dot infrared photodetector (SML QDIP) offers a fresh direction for this field of endeavor. A megapixel focal plane array based on SML QDIP has been successfully demonstrated. Finally, we showed that superlattice heterostructures, particularly those using unipolar barriers, can offer significant performance advantages over homojunction superlattices in infrared detection.

Acknowledgment

The authors thank J. Zmuidzinas, X. Cartoixà, and J. N. Schulman for helpful discussions, and M. Tidrow, R. Liang and P. Dimotakis for encouragement and support. The research described in this publication was sponsored in part by the JPL Research and Technology Development Program and by the Missile Defense Agency, and was carried out at the Jet Propulsion Laboratory, California Institute of Technology, under a contract with the National Aeronautics and Space Administration.

REFERENCES

1. M. Graf, G. Scalari, D. Hofstetter, J. Faist, H. Beere, E. Linfield, D. Ritchie, and G. Davies, "Terahertz range quantum well infrared photodetector," *Appl. Phys. Lett*. **84**(4), 475-477 (2004).

2. A. G. U. Perera, S. G. Matsik, B. Yaldiz, H. C. Liu, A. Shen, M. Gao, Z. R. Wasilewski, and M. Buchanan, "Heterojunction wavelength-tailorable far-infrared photodetectors with response out to 70 μm," *Appl. Phys. Lett*. **78**(15), 2241-2243 (2001).

3. A. B. Weerasekara, M. B. M. Rinzan, S. G. Matsik, A. G. U. Perera, M. Buchanan, H. C. Liu, G. von Winckel, A. Stintz, S. Krishna, "Si doped GaAs/AlGaAs terahertz detector and phonon effect on the responsivity," *Infrared Phys. Technol*. **50**(2-3), 194-198 (2007).

4. H. C. Liu, C. Y. Song, A. J. SpringThorpe, J. C. Cao, "Terahertz quantum-well photodetectors," *Infrared Phys. Technol*. **47** (1-2), 169-174 (2005).

5. H. Luo, H.C. Liu, C. Y. Song, and Z. R. Wasilewski, "Background-limited terahertz quantum-well photodetectors," *Appl. Phys. Lett*. **86**, 231103 (2005).

6. D. Z.-Y. Ting, Y.-C. Chang, S. V. Bandara, S. D. Gunapala, "Quantum well intrasubband photodetector for far infrared and terahertz radiation detection," *Appl. Phys. Lett*. **91** (7), 073510 (2007).

7. D. Z.-Y. Ting, Y.-C. Chang, S. V. Bandara, S. D. Gunapala, "Far infrared and terahertz quantum well intra-subband photodetector (QWISP)", *Proc. of SPIE*. **6660**, 66600F (2007).

8. D. Z.-Y. Ting, Y.-C. Chang, S. V. Bandara, S. D. Gunapala, "Quantum well intrasubband photodetector (QWISP): Prospects for large-format far-infrared focal plane arrays," *Proc. of SPIE* **6940,** 694006 (2008).

9. S. D. Gunapala and K. M. S. V. Bandara, *Physics of Thin Films*, Academic Press, **21**, 113 (1995).

10. H. Luo, H.C. Liu, C. Y. Song, and Z. R. Wasilewski, "Background-limited terahertz quantum-well photodetector," *Appl. Phys. Lett*. **86**, 231103 (2005).

11. D.Z.-Y. Ting, Y.-C. Chang, S.-V. Bandara, C. J. Hill, S.D. Gunapala, "Band structure and impurity effects on optical properties of quantum well and quantum dot infrared photodetectors," *Infrared Phys. Technol*. **50** (2-3), 136-141 (2007).

12. See M. Helm, in "Intersubband Transition in Quantum Wells: Physics and Device Applications I", ed. H. C. Liu and F. Capasso, Semiconductors and Semimetals **62** (Academic, New York, 2000), Chpt. 1, pp. 1–99.

13. K. M. S. V. Bandara, D. D. Coon, B. O, Y. F. Lin, and M . H. Francombe, "Exchange interaction in quantum well subbands," *Appl. Phys. Lett*. **53**(20), 1931-1933 (1988).

14. K. M. S. V. Bandara, D. D. Coon, B. O, Y. F. Lin, and M . H. Francombe, "Erratum: Exchange interaction in quantum well subbands [Appl. Phys. Lett. 53,1931 (1988)]," *Appl. Phys. Lett*. **55**(2), 206-208 (1989).

15. J. Phillips, "Evaluation of the fundamental properties of quantum dot infrared detectors," *J. Appl. Phys*. **91**, 4590-4594 (2002).

16. V. Ryzhii, I. Khmyrova, M. Ryzhii, and V. Mitin, "Comparison of dark current, responsivity and detectivity in different intersubband infrared photodetectors," *Semicond. Sci. Technol*. **19** (1), 8-16. (2004)

17. I. N. Stranski and L. Krastanow, Sitzungsberichte der Akademic der Wissenschaften in Wien, Mathematisch-Naturwissenschaftliche Klasse **146** (1937) 797.

18. N. N. Ledentsov, I. L. Krestnikov, M. Strassburg, R. Engelhardt, S. Rodt, R. Heitz, U. W. Pohl, A. Hoffmann, D. Bimberg, A. V. Sakharov, W. V. Lundin, A. S. Usikov, Z. I. Alferov, D. Litvinov, A. Rosenauer, and D. Gerthsen, "Quantum dots formed by ultrathin insertions in wide-gap matrices," *Thin Solid Films* **367**(1-2), 40-47 (2000).

19. Z. C. Xu, D. Birkedal, J. M. Hvam, Z. Y. Zhao, Y. M. Liu, K. T. Yang, A. Kanjilal, and J. Sadowski, "Structure and optical anisotropy of vertically correlated submonolayer InAs/GaAs quantum dots," *Appl. Phys. Lett*. **82**(22) 3859-3861 (2003).

20. F. Hopfer, A. Mutig, M. Kuntz, G. Fiol, D. Bimberg, N. N. Ledentsov, V. A. Shchukin, S. S. Mikhrin, D. L. Livshits, I. L. Krestnikov, and A. R. Kovsh, "Single-mode submonolayer quantum-dot vertical-cavity surface-emitting lasers with high modulation bandwidth," *Appl. Phys. Lett*. **89**(14) 141106 (2006).

21. T. D. Germann, A. Strittmatter, J. Pohl, U. W. Pohl, D. Bimberg, J. Rautiainen, M. Guina, and O. G. Okhotnikov, "High-power semiconductor disk laser based on InAs/GaAs submonolayer quantum dots," *Appl. Phys. Lett*. **92**(10) 101123 (2008).

22. I. L. Krestnikov, N. N. Ledentsov, A. Hoffmann, and D. Bimberg, "Arrays of two-dimensional islands formed by submonolayer insertions: Growth, properties, devices ," *Phys. Stat. Sol*. (a) **183** (2) (207-233 (2001).

23. V. A. Shchukin, N. N. Ledentsov, and D. Bimberg, *Epitaxy of Nanostructures*, Berlin Heidelberg: Springer-Verlag (2004).

24. V.A. Shchukin, D. Bimberg, "Self-ordering in multisheet arrays of 2D strained islands," *Thin Solid Films* 357(1) 66-70 (1999).

25. S.D. Gunapala, S.V. Bandara, C.J. Hill, D.Z. Ting, J.K. Liu, S.B. Rafol, E.R. Blazejewski, J.M. Mumolo, S.A. Keo, S. Krishna, Y.-C. Chang, and C. A. Shott, "640 x 512 pixels long-wavelength infrared (LWIR) quantum-dot infrared photodetector (QDIP) imaging focal plane array," *IEEE J. Quantum Electronics* , **43**(3), 230-237 (2007).

26. S. D. Gunapala and S. V. Bandara, in *Semiconductors and Semimetals*, New York: Academic, 1999, vol. 62, pp. 197–282.

27. K. K. Choi, K. L .Bacher and Y. Wu, "Corrugated QWIP with dielectric coverage for focal plane array applications," *Electrochemical Soc. Proc*. **98-21**, 71-82 (1998).

28. D. Z.-Y. Ting, S. V. Bandara, S. D. Gunapala, J. M. Mumolo, S. A. Keo, C. J. Hill, J. K. Liu, E. R. Blazejewski, S. B. Rafol, and Y.-C. Chang, "Submonolayer quantum dot infrared photodetector," *Appl. Phys. Lett*. **94**(11) 111107 (2009).

29. G. A. Sai-Halasz, R. Tsu, and L. Esaki, "A new semiconductor superlattice," *Appl. Phys. Lett*. **30**(12), 651-653 (1977).

30. L. Esaki and R. Tsu, "Superlattice and negative differential conductivity," *IBM J. Res. Dev*. **14**, 61-65 (1970).

31. J. H. Davies, *The Physics of Low Dimensional Semiconductors: An Introduction*, Cambridge University Press, Cambridge, New York, and Melbourne, 86-87 (1998).

32. D. Dragoman and M. Dragoman, Optical Characterization of Solids, Springer-Verlag, Berlin, Heidelberg and New York, 258-259 (2002).

33. G. A. Sai-Halasz, L. L. Chang, J.-M. Welter, C.-A. Chang and L. Esaki, "Optical absorption of $In_{1-x}Ga_xAs$-$GaSb_{1-y}As_y$ superlattices," *Solid State Commun. Phys*. **27**, 935-937 (1978).

34. J. N. Schulman and T. C. McGill, "The CdTe/Hg/Te superlattice: Proposal for a new infrared material," *Appl. Phys. Lett*. **34**(10), 663 (1979).

35. D. L. Smith, T. C. McGill, and J. N. Schulman, "Advantages of the HgTe-CdTe superlattice as an infrared detector material," *Appl. Phys. Lett*. **43**(2), 180 (1983).

36. D. L. Smith and C. Mailhiot, "Proposal for strained type II superlattice infrared detectors," *J. Appl. Phys.* **62**(6), 2545 (1987).

37. R. H. Miles, D. H. Chow, J. N. Schulman, and T. C. McGill, "Infrared characterization of $InAs/Ga_{1-x}In_xSb$ superlattices," *Appl. Phys. Lett*. **57**(8), 801 (1990).

38. D. H. Chow R. H. Miles, D. A. Collins, J. N. Schulman, and T. C. McGill, "Type-II superlattices for infrared detectors and devices," *Semicond. Sci. Technol.* **6**, C47-C51 (1991).

39. C. H. Grein, P. M. Young, and H. Ehrenreich, "Minority carrier lifetimes in ideal InGaSb/InAs superlattices," *Appl. Phys. Lett*. **61**(24), 2905 (1992).

40. E. R. Youngsdale, J. R. Meyer, C. A. Hoffman, F. J. Bartoli, C. H. Grein, P. M. Young, H. Ehrenreich, R. H. Miles, and D. H. Chow, "Auger lifetime enhancement in InAs-$Ga_{1-x}In_xSb$ superlattices," *Appl. Phys. Lett*. **64**(23), 3160 (1994).

41. Y.-C. Chang and J. N. Schulman, "Interband optical transitions in GaAs-$Ga_{1-x}Al_xAs$ and InAs-GaSb superlattices," *Phys. Rev. B* **31**(4), 2069 (1985).

42. R. H. Miles, J. N. Schulman, D. H. Chow and T. C. McGill, "Electronic band structure of far-infrared $Ga_{1-x}In_xSb$/InAs superlattices," *Semicond Sc. Technol. Phys.* **8**, S102-S105 (1993).

43. A. Y. Lew, S. L. Zuo, E. T. Yu, and R. H. Miles, "Correlation between atomic scale structure and mobility anisotropy in InAs/$Ga_{1-x}In_xSb$ superlattices," *Phys. Rev. B* **57**(11), 6534 (1998).

44. J. Steinshnider, J. Harper, M. Weimer, C.-H. Lin, S.-S. Pei, and D. H. Chow, "Origin of antimony segregatin in GaInSb/InAs strained-layer superlattices," *Phys. Rev. Lett.* **85**(21), 4562 (2000).

45. F. Fuchs, U. Weimer, W. Pletschen, J. Schmitz, E. Ahlswere, M. Walter, J. Wagner, and P. Koidl, "High-performance InAs/$Ga_{1-x}In_xSb$ superlattice infrared photodiodes," *Appl. Phys. Lett*. **71**(22), 3251 (1997).

46. P.-Y. Delaunay, B. M. Nguyen, D. Hoffman, E. K.-W. Huang, M. Razeghi, "Background Limited Performance of Long Wavelength Infrared Focal Plane Arrays Fabricated From M-Structure InAs-GaSb Superlattices," *IEEE J. Quant. Electron.* **45**(102), 157-162 (2009).

47. H. S. Kim, E. Plis, J. B. Rodriguez, G. D. Bishop, Y. D. Sharma, L. R. Dawson, S. Krishna, J. Bundas, R. Cook, D. Burrows, R. Dennis, K. Patnaude, A. Reisinger, and M. Sundaram, "Mid-IR focal plane array based on type-II InAs/GaSb strain layer superlattice detector with nBn design," *Appl. Phys. Lett*. **92**(18), 183502 (2008).

48. C. L. Canedy, E. H. Aifer, I. Vurgaftman, J. G.Tischler, J. R. Meyer, J. H.Warner, E. M. Jackson, "Antimonide type-II "W" photodiodes with long-wave infrared R_0A comparable to HgCdTe, *J. Electronic Materials* **36**(8), 852-856 (2007).

49. M. Walther, R. Rehm, J. Fleissner, J. Schmitz, J. Ziegler, W. Cabanski, and R. Breiter, "InAs/GaSb type-II short-period superlattices for advanced single and dual-color focal plane arrays," *Proc. SPIE* **6542**, 654206 (2007).

50. C. J. Hill, A. Soibel, S. A. Keo, J. M. Mumolo, S. D. Gunapala, D. R. Rhiger, R. E. Kvaas, and S. F. Harris," Infrared imaging arrays based on superlattice photodiodes, " *Proc. SPIE* **6940**, 69400C (2008).

51. H. J. Haugan,F. Szmulowicz, G. J. Brown, and K. Mahalingam, " Band gap tuning of InAs/GaSb type-II superlattices for mid-infrared detection," *J. Appl. Phys. Lett*. **96**(5), 2580-2585 (2004).

52. H. Mohseni, E. Michel, M. Razeghi, W. Mitchel, and G. Brown, "Growth and characterization of InAs/GaSb type II superlattices for long-wavelength infrared detectors," *Proc. SPIE* **3287**, pp.30-37 (1998).

53. X. Cartoixà, D. Z.-Y. Ting, and T. C. McGill," Description of bulk inversion asymmetry in the effective-bond-orbital model," *Phys. Rev. B* **68**(23), 235319 (2003)

54. J. Nguyen, D. Z.-Y. Ting, C. J. Hill, A. Soibel, and S. D. Gunapala, "Dark current analysis of InAs/GaSb superlattices at low temperatures," to appear in *Infrared Phys. Technol*.

55. H. Kroemer, "A proposed class of heterojunction injection lasers," *Proc. IEEE* **51**(12), 1782 (1963).

56. Zh. I. Alferov, R. F. Kazarinov, Inventor's Certificate No. 181737 (in Russian), Application No. 950 840 (1963).

57. A. M. White, "Infra red detectors," USA Patent 4,679,063 (1987).

58. M. Carras, J. L. Reverchon, G. Marre, C. Renard, B. Vinter, X. Marcadet, and V. Berger, "Interface band gap engineering in InAsSb photodiodes," *Appl. Phys. Lett*. **87**(10) 102103 (2005)

59. S. Maimon and G. W. Wicks, "nBn detector, an infrared detector with reduced dark current and higher operating temperature," *Appl. Phys. Lett*. **89**(15) 151109 (2006).

60. J. R. Pedrazzani, S. Maimon and G. W. Wicks, "Use of nBn structures to suppress surface leakage currents in unpassivated InAs infrared photodetectors," *Electronics Lett*. **44**(25) 1487-1488 (2008).

61. P. Klipstein, "'XBn' barrier photodetectors for high sensitivity and high operating temperature infrared sensors," *Proc. of SPIE*. 6940 (2009) 69402U.

62. J. B. Rodriguez, E. Plis, G. Bishop, Y. D. Sharma, H. Kim, L. R. Dawson, and S. Krishna, "nBn detectors based on InAs/GaSb type-II strain layer superlattice," *Appl. Phys. Lett*. **91**(4) 043514 (2007).

63. J. L. Johnson, L. A. Samoska, and A. C. Gossard, J. L. Merz, M. D. Jack, G. R. Chapman, B. A. Baumgratz, K. Kosai, and S. M. Johnson, "Electrical and optical properties of infrared photodiodes using the InAs/$Ga_{1-x}In_xSb$ superlattice in heterojunctions with GaSb," *J. Appl. Phys. Lett*. **80**(2) 1116-1127 (1996).

64. B.-M. Nguyen, D. Hoffman, E. K.-W. Huang, P.-Y. Delaunay, and M. Razeghi, "Background limited long wavelength infrared type-II InAs/GaSb superlattice photodiodes operating at 110 K," *Appl. Phys. Lett*. **93**(12) 123502 (2008).

65. I. Vurgaftman, E. H. Aifer, C. L. Canedy, J. G. Tischler, J. R. Meyer, J. H. Warner, E. M. Jackson, G. Hildebrandt and G. J. Sullivan, "Graded band gap for dark-current suppression in long-wave infrared W-structured type-II superlattice photodiodes," *Appl. Phys. Lett*. **89**(12), 121114 (2006).

66. D. Z.-Y. Ting, C. J. Hill, A. Soibel, S. A. Keo, J. M. Mumolo, J. Nguyen, and S. D. Gunapala, unpublished.